doi:10.26443/seismica.v4i2.1660

3D Converted Wave Reverse Time Migration Imaging

Leah Langer * [1], **Chris Henze** [2], **Fred F. Pollitz** [3], **Jeffrey J. McGuire** [3]

[1]Department of Geophysics, Tel Aviv University, Tel Aviv, Israel, [2]NASA Ames Research Center, Moffett Field, CA, USA, [3]U.S. Geological Survey, Moffett Field, CA, USA

Author contributions: *Conceptualization*: Fred F. Pollitz, Jeffrey J. McGuire, Leah Langer. *Methodology*: Fred F. Pollitz. *Software*: Chris Henze. *Investigation*: Leah Langer. *Writing - Original draft*: Leah Langer. *Visualization*: Chris Henze. *Supervision*: Jeffrey J. McGuire.

Abstract We describe a newly developed method for recovering high-resolution images of seismic discontinuities, such as subducting slabs, in 3D. Our method makes use of converted $S \rightarrow P$ or $P \rightarrow S$ waves observed by dense arrays of seismometers to infer the locations and relative strengths of seismic discontinuities at depth in a target region. Observed direct and converted waves are backpropagated to their times of origin. The time-reversed wavefield is then separated into its constituent P and S components via the Helmholtz decomposition, and those separated wavefields are used to compute imaging functions that characterize the locations and relative strengths of seismic discontinuities. Imaging functions may be designed to use either $S \rightarrow P$ or $P \rightarrow S$ waves, so that users can target those arrivals expected to be most dominant in a given dataset. We have previously demonstrated the efficacy of our method in two dimensions, and we now present a 3D implementation of our technique which addresses the significant computational challenges posed by the size of volumetric wavefield data in three dimensions. Through a series of synthetic examples, we demonstrate that our method is capable of recovering the fine scale structure of a subducting slab given realistic station coverage and earthquake sources. We investigate optimal seismic station geometries for our technique and explore image interpretability in regions with poor data coverage. We find that linear station geometries yield more optimal, interpretable imaging functions than collections of small arrays can. We also show that our method can successfully recover both $S \rightarrow P$ or $P \rightarrow S$ images when realistic shear earthquake sources are used, and we explore the additional computational challenges presented by the high frequency content of S waves. Our results demonstrate the potential for our technique to recover high-resolution information about subducting slabs in real-world regions, given that relatively sparse seismic arrays with only approximately 100 stations are capable of recovering interpretable imaging functions from just a few realistic earthquake sources for multiple discontinuities at significant depth in an area of approximately 400 sq km.

Production Editor:
Gareth Funning
Handling Editor:
Chiara Civiero
Copy & Layout Editor:
Théa Ragon

Signed reviewer(s):
David Schlaphorst

Received:
April 1, 2025
Accepted:
November 17, 2025
Published:
December 3, 2025

1 Introduction

High-resolution imaging of a seismic discontinuity, such as a subducted slab, may be accomplished using converted S to P or P to S waves. This type of analysis has successfully been used in subducted slab imaging studies in many regions around the world (e.g., Eberhart-Phillips and Reyners, 1999; Horleston and Helffrich, 2012; Gong and McGuire, 2021). More precise imaging with converted waves has been investigated via reverse time migration (RTM) methods, in which direct and converted waves observed on the Earth's surface are back-propagated to the location of discontinuities. The direct and converted time-reversed wavefields may then be cross-correlated to obtain an estimate of the discontinuity's location (e.g. Shang et al., 2012; Duan and Sava, 2015; Shabelansky et al., 2017; Li and Li, 2022). These methods utilize high-frequency seismic data from local earthquakes to obtain high-resolution images of a seismic discontinuity. A recent study, Zou et al. (2024), successfully demonstrated the capacity of this type of technique to obtain images of the subducting slab in southwest Japan.

Here, we present a 3D implementation of our converted wave RTM imaging technique. The method is intended to target dense seismic datasets collected in subduction zone regions. Our algorithm (Langer et al., 2023) is based on an approach that is conceptually similar to the methods presented by Duan and Sava (2015); Shabelansky et al. (2017), and Du et al. (2019). Direct and converted waves are back-propagated to their point of origin and separated into their constituent P and S components using the Helmholz decomposition, and those time-reversed wavefields are then used to construct an imaging function. Our method differs from previous work because the computed imaging functions feature high signal-to-noise ratio, and under some circumstances, an interpretable imaging function may be obtained with data from only a single earthquake. Our imaging functions are also normalized to remove any dependence on the seismic wavefields that were used to construct them, which means that the images may be used to infer the relative strengths of impedance contrasts (that is, the contrast in seismic shear velocity and density across a boundary) as well as their locations.

The 3D high-resolution structural information provided by our imaging functions represents a large step

*Corresponding author: llanger@tauex.tau.ac.il

forward in comparison with current structural models utilized by dynamic rupture and ground motion simulations. While 2D models of dynamic rupture (coupled with tsunami generation) yield valuable insights into first-order structural controls on cascading hazards (e.g. Lotto et al., 2019), 3D models of these processes are feasible (e.g. Kutschera et al., 2024; Madden et al., 2020), but they are contingent upon the availability of 3D structural models. Appropriate 3D structural models are rarely available as inputs for dynamic rupture and ground motion studies in subduction zone regions, because while high resolution seismic imaging is achievable offshore via active source seismic imaging studies (Preston et al., 2003; Shiraishi et al., 2019), onshore imaging, which generally relies on passive source seismic data, often from teleseismic earthquakes, is of far lower resolution, with an upper frequency limit of approximately 0.5 Hz (Bostock et al., 2001; Nikulin et al., 2009). Very high density arrays in receiver function analysis permit potentially higher frequency analysis and finer resolution of structure at depth (Ward et al., 2018), but this isn't common practice due to limitations on the types of earthquake sources which can be used and the need to utilize very small windows, which may allow for imaging only of shallow structure above the slab interface. In addition, it is not clear how signal-generated noise, including expected high levels of scattering of teleseismic waves from small-scale heterogeneities (e.g. Takemura et al., 2015), impact these results. Our technique, which utilizes local earthquake sources, avoids these issues.

High-resolution imaging of the structure of subducting slabs, particularly shear structure, is important because variations in thickness and extent of low seismic velocity layers within the slab are believed to strongly impact rupture dynamics and extent. Fault zones are often contained within areas of relatively low seismic velocity. In subduction zones, the low velocity layers correspond to fluid rich subducted sediment in both the shallow updip part of the fault (Bangs et al., 2023) and down through seismogenic zone depths where active source imaging has been possible (Nedimovic et al., 2003; Li et al., 2015). Changes in the thickness of this subducted sediment layer may delineate rheological changes and hence have first order implications for estimating the downdip rupture extent and hazard from future large earthquakes (Nedimovic et al., 2003). Similarly, along-strike variations in the thickness of the subducted sediment layer are correlated with the extents of past great earthquakes (Contreras-Reyes and Carrizo, 2011; Bassett et al., 2025), indicating a potential control on rupture dynamics. Low velocity zones trap seismic energy, particularly shear waves, and are capable of having a first-order effect on the dynamic stress field during rupture (Duan, 2008; Huang and Ampuero, 2011; Thakur et al., 2020). At and below the base of the seismogenic zone, the presence of high Vp/Vs ratio zones and/or low velocity zones are key to understanding the physical mechanisms that control interseismic locking (Guo et al., 2021) and slow slip. Imaging methods based on converted waves may be capable of providing information about the temporal evolution of fluid content (Herath and Audet, 2024), allowing comparisons with slow slip cycles. Understanding the connections between long-term rupture behavior, slow slip, and material properties in the vicinity of the megathrust at depths of 20-40 km requires much higher resolution information than can currently be obtained through onshore imaging methods, and is a target of key research plans (Gomberg et al., 2017). To achieve this, methods are needed that approach the frequency band typically utilized for active source reflection imaging, approximately 5-15 Hz (Li et al., 2015). Our converted-wave RTM technique is capable of recovering high-resolution onshore structural information thanks to its use of seismic data from local earthquake sources. Imaging functions recovered by our technique can potentially approach the lower end of the active source imaging frequency band with typical waveforms from magnitude M2.0 – M4.0 earthquakes in the downgoing plate, and thus allow high-resolution imaging of megathrust fault zones in regions where active source studies are impractical.

In our prior publication, Langer et al. (2023), we presented a 2D implementation of our technique and showed the potential of our newly developed method to recover high resolution images of subducting slabs onshore. We have now developed a 3D implementation, which will give us great flexibility in using our method in real-world settings. Our new implementation will enable us to image detailed along-strike structure in subduction zones, and will eliminate error introduced when non-planar earthquake and station geometries are projected onto a plane during 2D imaging. Although the theoretical framework we previously developed translates easily to three dimensions, a 3D implementation presents significant computational challenges. The volumetric computed 3D wavefields are very large, and lead to substantial memory and data storage requirements that must be addressed when computing imaging functions and producing visualizations of the wavefield and imaging data.

In this study, we describe solutions that we developed to address these computational challenges and present a workflow of the 3D implementation of our technique. We then illustrate the method with synthetic examples that demonstrate its applicability in regions with subduction zone like structure, and show that our imaging functions are able to recover the target structure using data from realistic earthquake sources. We also explore the effects of seismic station geometry on image interpretability, and discuss optimal station geometries for arrays that are designed to target this type of seismic imaging technique.

2 Methods

2.1 Theoretical Treatment

A summary of our method is presented here. We refer the reader to Appendix A of Langer et al. (2023) for a complete theoretical treatment of our converted wave reverse time migration imaging method. The theoretical treatment is the same in two or three dimensions;

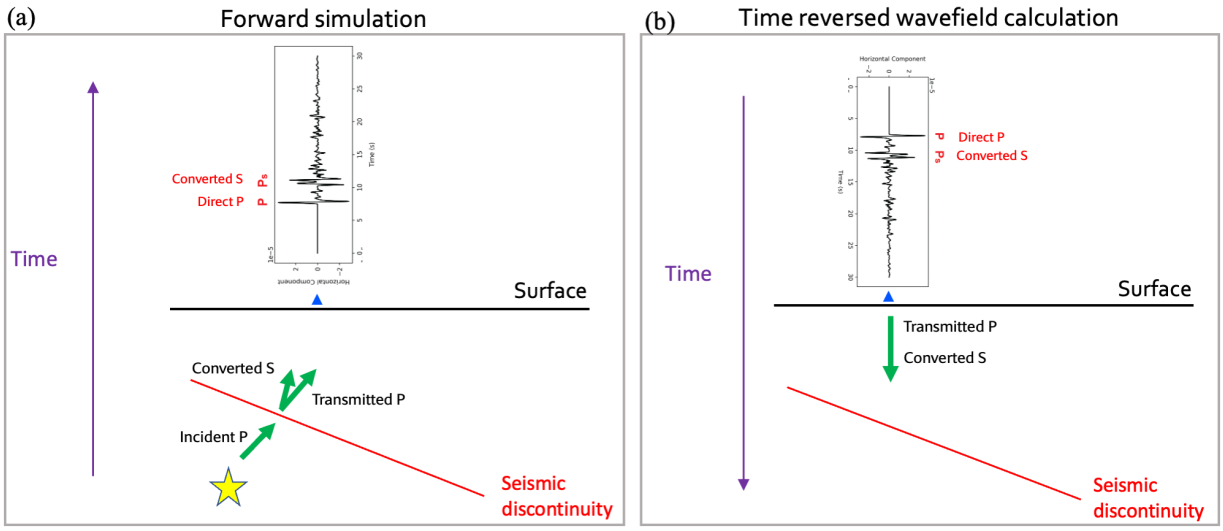

Figure 1 Conceptual illustration of converted wave imaging. In this example, in panel (a), an incident P wave emanating from an earthquake source interacts with a boundary at depth to produce a transmitted direct P wave and a converted $P \rightarrow S$ wave. A single seismic station at the location of the blue dot records these phases. In panel (b), the seismogram is time reversed in an adjoint simulation. During the adjoint simulation, the end of the seismogram is injected first, so the converted S wave is backpropagated into the domain prior to the direct P wave. The faster velocity P wave and slower velocity S wave are temporally co-located when both phases reach the seismic discontinuity.

however, the code implementation is slightly different because it is necessary for all vector quantities to be specified in three rather than two dimensions.

As shown in Figure 1(a), when seismic waves originating from an earthquake source encounter a discontinuity at depth, converted ($P \rightarrow S$ and $S \rightarrow P$), reflected and transmitted waves are produced. All seismic waves may then be observed by an array of seismic receivers at Earth's surface. We assume that the seismic discontinuities may be characterized as specular discontinuities, and we portray the locations and strengths of those discontinuities using imaging functions that estimate the $P \rightarrow S$ and $S \rightarrow P$ wave conversion coefficients. To calculate these imaging functions, we first time reverse the recorded wavefields, as shown in Figure 1(b). The time reversed receiver wavefield is separated into its constituent P and S components using the Helmholtz decomposition:

$$\left(\mathbf{u}^{\ddagger}\right)_P = \alpha^2 \nabla \left(\nabla \cdot \mathbf{u}^{\ddagger}\right) \tag{1}$$

$$\left(\mathbf{u}^{\ddagger}\right)_S = -\beta^2 \nabla \times \left(\nabla \times \mathbf{u}^{\ddagger}\right) \tag{2}$$

where $\mathbf{u}^{\ddagger}$ is the time reversed receiver wavefield.

To determine the imaging function for a single earthquake source, we calculate a zero lag cross-correlation using the direct (transmitted) and converted receiver wavefields. Imaging functions from multiple earthquake sources are then stacked and normalized to give the final imaging function:

$$I_{P\rightarrow S}(\boldsymbol{\xi}) = \frac{1}{\alpha(\boldsymbol{\xi}) \sum_j p(\boldsymbol{\xi}, j)} \sum_j \frac{\int_0^T \left(\delta \mathbf{u}_j^{\ddagger}(\boldsymbol{\xi}, t) \cdot \hat{\mathbf{t}}\right)_S \left(\mathbf{u}_j^{\ddagger}(\boldsymbol{\xi}, t) \cdot \hat{\mathbf{n}}\right)_P dt}{\int_0^T \left|\left(\mathbf{u}_j^{\ddagger}(\boldsymbol{\xi}, t) \cdot \hat{\mathbf{n}}\right)_P\right|^2 dt} \tag{3}$$

$$I_{S\rightarrow P}(\boldsymbol{\xi}) = \frac{1}{\beta(\boldsymbol{\xi}) \sum_j p(\boldsymbol{\xi}, j)} \sum_j \frac{\int_0^T \left(\delta \mathbf{u}_j^{\ddagger}(\boldsymbol{\xi}, t) \cdot \hat{\mathbf{n}}\right)_P \left(\mathbf{u}_j^{\ddagger}(\boldsymbol{\xi}, t) \cdot \hat{\mathbf{t}}\right)_S dt}{\int_0^T \left|\left(\mathbf{u}_j^{\ddagger}(\boldsymbol{\xi}, t) \cdot \hat{\mathbf{t}}\right)_S\right|^2 dt} \tag{4}$$

In these formulas, j is the index of a particular earthquake source and $p(\boldsymbol{\xi}, j)$ is the ray parameter for the direct wavefield from source # j at $\boldsymbol{\xi}$. $\hat{\mathbf{n}}$ and $\hat{\mathbf{t}}$ are normal and tangent vectors to the hypothetical discontinuity at $\boldsymbol{\xi}$. $\hat{\mathbf{n}}$ and $\hat{\mathbf{t}}$ are calculated using the dip of the seismic discontinuity, which must be specified *a priori*. α and β are P and S velocities on a reference structure. In our implementation, the denominator $\int_0^T \left|\left(\mathbf{u}_j^{\ddagger}(\boldsymbol{\xi}, t) \cdot \hat{\mathbf{n}}\right)_P\right|^2 dt$ or $\int_0^T \left|\left(\mathbf{u}_j^{\ddagger}(\boldsymbol{\xi}, t) \cdot \hat{\mathbf{t}}\right)_S\right|^2 dt$ is laterally averaged to ensure numerical stability. The lateral averaging is performed by calculating the average of the value of the denominator over points within the $X - Y$ plane for each depth value in the mesh. Note that the method is source independent; no information about the focal mechanism or location are required.

These formulas are identical to those introduced in Langer et al. (2023), which presented a 2D implementation of this method. In that publication, it was shown that these imaging functions are proportional to the ratio of converted wave to direct wave transmission coefficients across a seismic discontinuity and that they are, to first order, dependent on the the contrast in density, $\Delta\rho$, and the contrast in shear velocity, $\Delta\beta$, across the discontinuity. This means that our imaging functions can be used to infer density contrast and shear wave structure, which are linked to porosity, fluid pressure, and sediment properties of a subducting slab (Christensen, 1996). These properties are believed to be most critical for understanding the probable extent and velocity of rupture, particularly downdip (Kato et al., 2010; Liu, 2013; den Hartog and Spiers, 2014).

2.2 Code Implementation and Workflow

Our workflow uses the SPECFEM3D wave propagation code (Komatitsch and Tromp, 2002a,b) to compute seismic wavefields due to forward and adjoint sources in a 3D structure. Imaging functions for a synthetic domain are computed as follows: A forward run of SPECFEM3D in the target velocity model is first used to obtain synthetic seismic data at specified station locations for a given earthquake source. This step would obviously not be necessary when calculating imaging functions with real seismic data. The seismic data are then filtered with a 3 Hz lowpass filter, and seismograms are windowed to eliminate interference from phases other than those of interest. Seismograms from each earthquake are then back propagated via an adjoint run of SPECFEM3D in a domain that contains the smoothed velocity model, which is obtained by utilizing a Guassian filter to smooth the target velocity model. During the adjoint run, 3D displacement and velocity data are saved for each Gauss-Lobatto-Legendre (GLL) quadrature point in the volume at every time step. We then compute the Helmholtz decomposition to separate the displacement and velocity wavefields into their constituent P and S components. These decomposed wavefields are then used to compute the imaging functions using the workflow illustrated in Figure 2.

This workflow features significant potential bottlenecks due to the size of datasets that are produced and analyzed to obtain an imaging function. During adjoint runs, we output three-component velocity and displacement data at every GLL point in the volume of the mesh at every time step. Initially, this step took a very long time (often several hours for large meshes) due to the size of the datasets being written to file. The datasets are very large because the mesh must be very fine in order to avoid artifacts at mesh elements that would otherwise result from the second order spatial derivatives required for the Helmholtz decomposition. We found that a mesh spacing of 50-60% of the S wavelength is needed to ensure that decomposed wavefields are smooth and artifact free, approximately half the mesh spacing typically required for seismic propagation codes. If the velocity structure is not homogeneous, variable mesh spacing may be utilized to reduce the overall number of elements, but the model will still include more GLL points than would be required for a typical seismic propagation model. For the examples presented in this study, the mesh contains nearly 2 million elements, with 5 GLL points per dimension in each element. The seismograms utilized in the adjoint runs are 15s long, with a time step of 0.0025s, for a total of 6,000 samples.

To address this issue, we developed a new I/O routine which minimizes time spent writing data to file. In our current workflow, at each time step, volumetric displacement and velocity data are sent to a processor that writes data to file while the remaining processors continue to perform calculations. This routine has led to a significant reduction in the time required to write the full wavefield data to file, from up to several hours to just minutes. The saved wavefield data are then used to compute the imaging function. The imaging function calculation follows the method presented in Langer et al. (2023); the only change required for 3D vs. 2D wavefields is that the normal and tangential vectors to the fault must be specified in three components.

3 Examples

In this section, we present imaging functions that are calculated with synthetic seismic data. The model domain and velocity structure used to generate these synthetic data are shown in Figure 3(a). This is the target model that we will attempt to recover with our imaging functions. The velocity model is designed to imitate the structure of a generic subduction zone region, with a low-velocity layer on the top of the slab and higher-velocity layers beneath it. The top of the slab features a square-shaped topographic bulge measuring 1 km high and 10×10 km wide. The height and scale of this bulge are similar to subducted seamounts that are imaged in the shallow parts of subduction zones due to seamounts. For instance, Carbotte et al. (2024) imaged seamounts that are approximately 1 to 2.5 km high and 5 to 8 km wide offshore of Oregon in the shallow part of the Cascadia subduction zone. Our model domain measures $40 \times 40 \times 45$ km. The smoothed velocity model utilized in backpropagation calculations is shown in Figure 3(b).

3.1 Isotropic earthquake sources

One important question that must be addressed is the issue of optimal station geometry for seismometer deployments targeting imaging function analysis. Theoretically, a dense grid of stations would be the best choice, because this would provide full coverage in all directions, enabling the backpropagated wavefronts to optimally cohere at depth. Unfortunately, this type of station geometry is not often achievable in the real world, due to limitations imposed by topography, vegetation, urban infrastructure, and permitting requirements. Therefore, we tested a variety of station geometries to determine the most optimal choice in a region with imposed limitations. The first station geometry is a theoretically optimal grid of 400 stations. The grid mea-

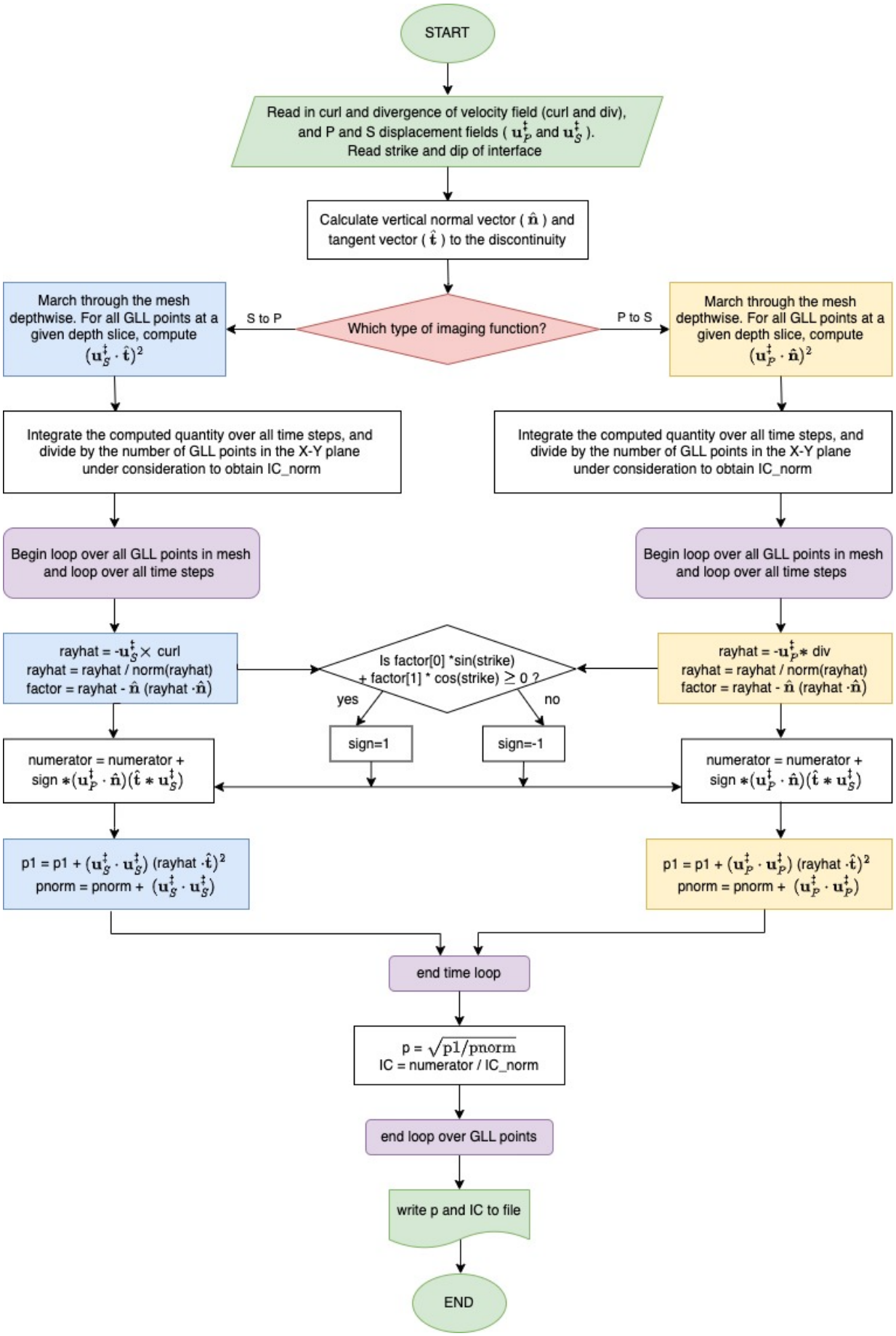

Figure 2 Imaging function code workflow

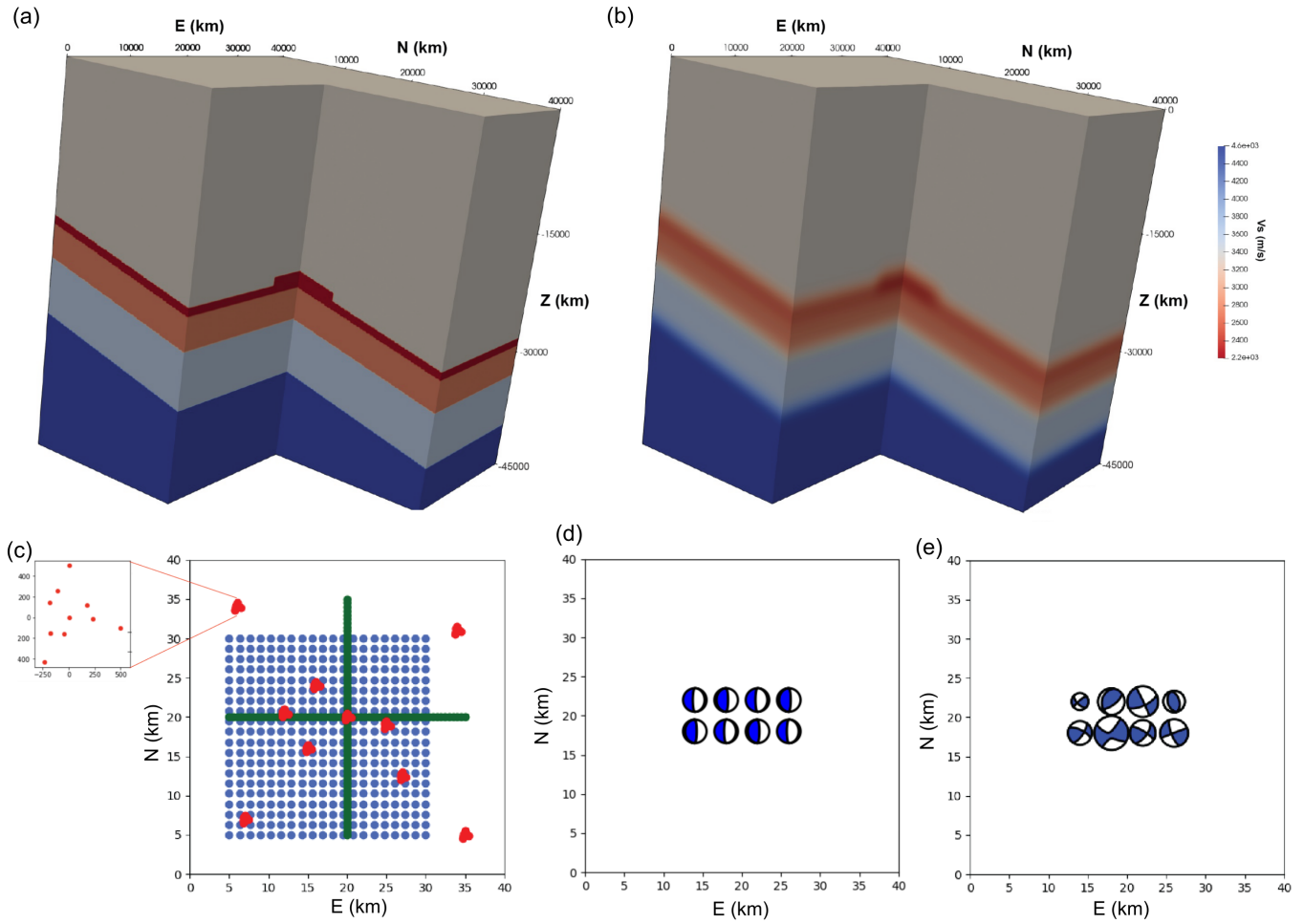

Figure 3 Model design for our examples. (a) true velocity structure used to calculate synthetic seismograms. (b) smoothed velocity structure used for our time reversed wavefield calculations. (c) Station geometry. Grid of stations shown as blue circles, perpendicular lines of stations in green and mini arrays in red. Inset shows the geometry of a single mini array. View is looking down in the surface of the domain. (d) and (e): earthquake source geometries. View is a 2D slice of the XY plane at 40 km depth. Earthquake sources in (d) are shear sources dipping $+75°$ and $-75°$. (e) shows earthquake source geometry for examples with realistic earthquake sources. The size of each beachball corresponds to the magnitude of that event.

sures 25 × 25 km and has a station spacing of 1.25 km. The second station geometry consists of two linear perpendicular lines, each 30 km long with a station spacing of .5 km for a total of 120 stations. The third station geometry consists of 10 mini-arrays, each with 10 stations in an area of approximately 1 sq km. Both of these types of geometries could be realized for our frequency band using temporary deployments of nodal seismometers or other instruments. Additionally, several 'array of arrays' datasets exist (Ghosh et al., 2009; Ryberg et al., 2010; Hutchison and Ghosh, 2017). The three station geometries are shown in Figure 3(c). The locations of the synthetic events are shown in Figure 3(d). All of the earthquakes are at 40 km depth. For each of the 8 earthquakes shown in this figure, we assigned an isotropic moment tensor and generated synthetic data at all of the station locations for the three station geometries by performing a forward calculation in the target model shown in Figure 3(a). The seismic data for each of the station geometries were then filtered as described in Section 2.2 and backpropagated in the smoothed model shown in Figure 3(b), and an imaging function given by Equation 3 was calculated for that station geometry and earthquake. Then, for each of our chosen station geometries, we stacked the imaging functions for all eight earthquakes and normalized to obtain the results shown in Figure 4. Movies showing the full 3D imaging functions are included in the Supplementary Material.

In these figures, bright red lines represent strongly positive locations in the imaging function, while bright blue lines represent strongly negative locations in the imaging function. The sign of the imaging function corresponds to the sign of the velocity difference across a discontinuity; because the uppermost discontinuity represents a change from a higher velocity region above to a lower velocity region below, while all other discontinuities represent a jump in velocity values from above to below, we expect the imaging function for the uppermost discontinuity to have the opposite sign of all others, which it does. The imaging function for each discontinuity has side lobes of the opposite sign, consistent with the narrow band nature of the time reversed waveforms. All of the stacked imaging functions recover interpretable information about each of the significant seismic discontinuities present in our structure. The shape of the upper surface of the slab is represented

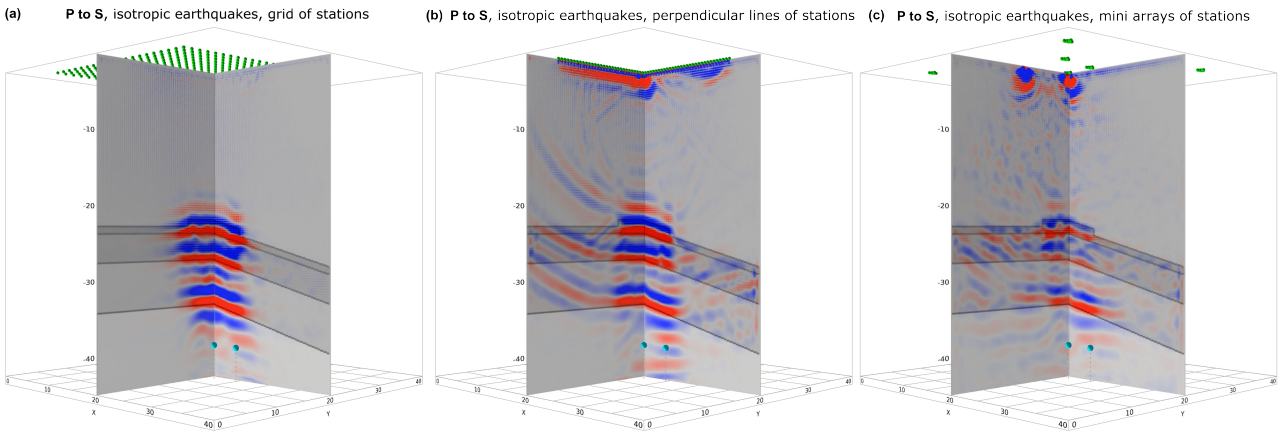

Figure 4 Stacked $P \rightarrow S$ imaging functions with 8 isotropic earthquake sources for each of the three station geometries. (a) imaging function for grid of 400 seismic stations. (b) imaging function for two perpendicular lines of stations. (c) imaging function for 10 mini arrays.

well, showcasing the capability of our technique to recover fine-scale structure with good fidelity.

As expected, the grid of seismic stations recovers the most optimal imaging function, with very few artifacts and bright, clean curves clearly marking the locations of each of the significant discontinuities across a large area. The imaging function is only recovered near the raypaths to the receivers from the earthquakes, which are clustered near the center of the domain, with minimal artifacts outside the resolvable region. By contrast, Figure 4(b), which shows the imaging function recovered by two perpendicular lines of stations, features significant artifacts outside the resolvable region. However, this imaging function has promising features as well; despite the relative sparsity of stations, recovery of the imaging function in the resolvable region near the center of the domain is excellent, and the movie presented in the Supplementary Material shows that the structure is well resolved within a region approximately 5 km around the array. One can readily deduce the interpretable region of this imaging function through analysis of source-receiver raypaths. Similarly, the imaging function recovered by 10 mini arrays, shown in Figure 4(c), includes artifacts outside the resolvable area, but near the center of the domain, it is able to recover the structure surprisingly well, given the sparsity of the coverage for this array as shown in Figure 3(c). These results demonstrate that our technique is capable of recovering interpretable imaging functions for multiple discontinuities at depth in a large area of approximately 400 sq km using data from only 8 earthquakes and a relatively sparse seismic array.

3.2 Synthetic shear earthquake sources

Our tests with isotropic earthquakes established that informative imaging functions may be obtained with realistic station geometries. To extend the method to more realistic earthquake sources, which produce more complex wavefields, we first attempt to recover an $S \rightarrow P$ imaging function from synthetic data generated from 75-degree dipping shear earthquake sources. The locations of these earthquakes is the same as in the isotropic earthquake test cases, but now 50% of the earthquake sources are shear sources dipping 75° east and 50% of the earthquake sources are shear sources dipping 75° west. The locations of these sources is as shown in Figure 3(d). Synthetic seismic data were generated at the grid of 400 stations for each of these earthquakes via a forward run of SPECFEM3D in the target velocity structure shown in Figure 3. The data were then filtered with a 3 Hz lowpass filter, and windowed to remove interference from phases other than those of interest. The latter step is important when processing data from shear sources because the seismograms from these earthquakes are more complex, and include many phases which tend to interfere positively when imaging functions are calculated from backpropagated data, leading to artifacts. To best isolate the $S \rightarrow P$ imaging function, we window the data to remove the direct P wave and all information after the direct S wave. This process improves the signal-to-noise ratio for $S \rightarrow P$ imaging functions, which are formed by cross-correlation of direct S and converted $S \rightarrow P$ seismic phases.

When the filtering and windowing processes are complete, the seismic data from each earthquake were backpropagated in the smoothed velocity structure shown in Figure 3(b), and the imaging function was calculated from the backpropagated wavefields. Imaging functions from all eight earthquakes were then stacked and normalized to obtain the final result shown in Figure 5. Movies showing the full 3D imaging functions are included in the Supplementary Material.

This imaging function is bright at all significant discontinuities recovered by the $P \rightarrow S$ imaging functions shown in Figure 4 for isotropic earthquake sources. It additionally recovers another, very fine scale seismic discontinuity that is not recovered by our $P \rightarrow S$ imaging functions: the 1 km thick discontinuity marking the base of the uppermost layer of the slab. It is not surprising that $S \rightarrow P$ imaging functions are capable of recovering higher-resolution images, due to the shorter wavelengths of S waves. However, there is a tradeoff to this higher resolution capability. The imaging function displayed in Figure 5 shows high-resolution artifacts at each of the discontinuities present in our struc-

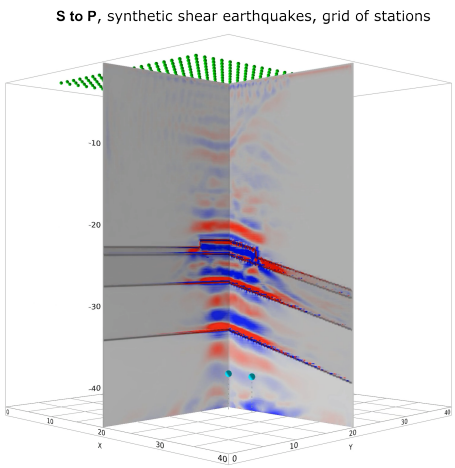

Figure 5 Stacked $S \rightarrow P$ imaging function for shear sources dipping $75°$.

ture. As with the artifacts present in imaging functions obtained with nonoptimal station geometries, these artifacts should be anticipated and accounted for during interpretation of imaging functions.

3.3 Realistic earthquake sources

As final evidence of our technique's capability to produce informative imaging functions in a realistic setting, we selected eight earthquake sources from the Gorda region of the Cascadia subduction zone and calculated an imaging function with synthetic data generated from those earthquake sources. The earthquake sources have magnitudes between M2.7 – M5.4, and were selected from the aftershock sequence of December 2022 M6.4 Ferndale earthquake. The moment tensors and locations for each earthquake are shown in Figure 3(e). These locations are identical to those used for synthetic isotropic and shear sources in our previous examples, and do not correspond to real-world earthquake locations. Synthetic seismograms were calculated via a forward run of SPECFEM3D for each earthquake source in the target model domain shown in Figure 3(a). The synthetic seismograms, earthquake sources and station information for this dataset can be found in the USGS data release (Langer, 2024). The seismograms were then filtered with a 3 Hz lowpass Butterworth filter, and windowed to remove interference from seismic phases other than those of interest. The windowing scheme for these seismograms is shown in Figure 6: prior to adjoint runs intended for $P \rightarrow S$ imaging function calculations, the direct S wave and everything after it were removed from the record section; and prior to adjoint runs intended for $S \rightarrow P$ imaging function calculations, the direct P wave and all data after the direct S wave were removed.

The processed seismograms were backpropagated via an adjoint run of SPECFEM3D in a domain with the smoothed velocity structure shown in Figure 3(b). Imaging functions were then calculated for each earthquake. The $P \rightarrow S$ and $S \rightarrow P$ imaging functions were then separately stacked and normalized. For these earthquake sources, we computed imaging functions for two station geometries: the grid of 400 stations and the two perpendicular lines of 120 total stations. Figure 7 shows stacked $P \rightarrow S$ and $S \rightarrow P$ imaging functions obtained with synthetic seismic data from the grid of 400 stations. Movies showing the full 3D imaging functions are included in the Supplementary Material.

These stacked imaging functions are consistent with each other and with results found with synthetic earthquake sources. The $P \rightarrow S$ imaging function shows that all significant seismic discontinuities are recovered well, with bright, clean curves clearly delineating the locations of the discontinuities and the shape of the top of the slab recovered correctly. As expected, the imaging function at the top of the slab is opposite in sign from the imaging function indicating the locations of deeper seismic discontinuities. This sign difference is consistent with the difference in velocity change across the discontinuities; as we have previously discussed, the uppermost discontinuity represents a velocity contrast that is opposite in sign to the velocity contrast represented by the lower discontinuities. The $S \rightarrow P$ imaging function is consistent with the $P \rightarrow S$ imaging function, and is also very clean, with minimal artifacts, but it recovers information in a smaller region near the center of the domain. This is to be expected, because S waves have higher takeoff angles and therefore illuminate a smaller region as their raypaths are concentrated near the source. This $S \rightarrow P$ imaging function, similarly to the $S \rightarrow P$ imaging function recovered with synthetic shear sources, is able to recover the additional fine-scale seismic discontinuity at the base of the slab surface that is not recovered by our $P \rightarrow S$ imaging functions.

In order to fully establish the capability of our imaging technique to recover velocity structure in a realistic setting, we calculated $P \rightarrow S$ and $S \rightarrow P$ imaging functions for the Gorda earthquake sources using seismic data from the array with two perpendicular lines of stations and 120 total stations. The stacked imaging functions are shown in Figure 8. Movies showing the full 3D imaging functions are included in the Supplementary Material.

These imaging functions, too, are consistent with results found with synthetic earthquake sources, and with

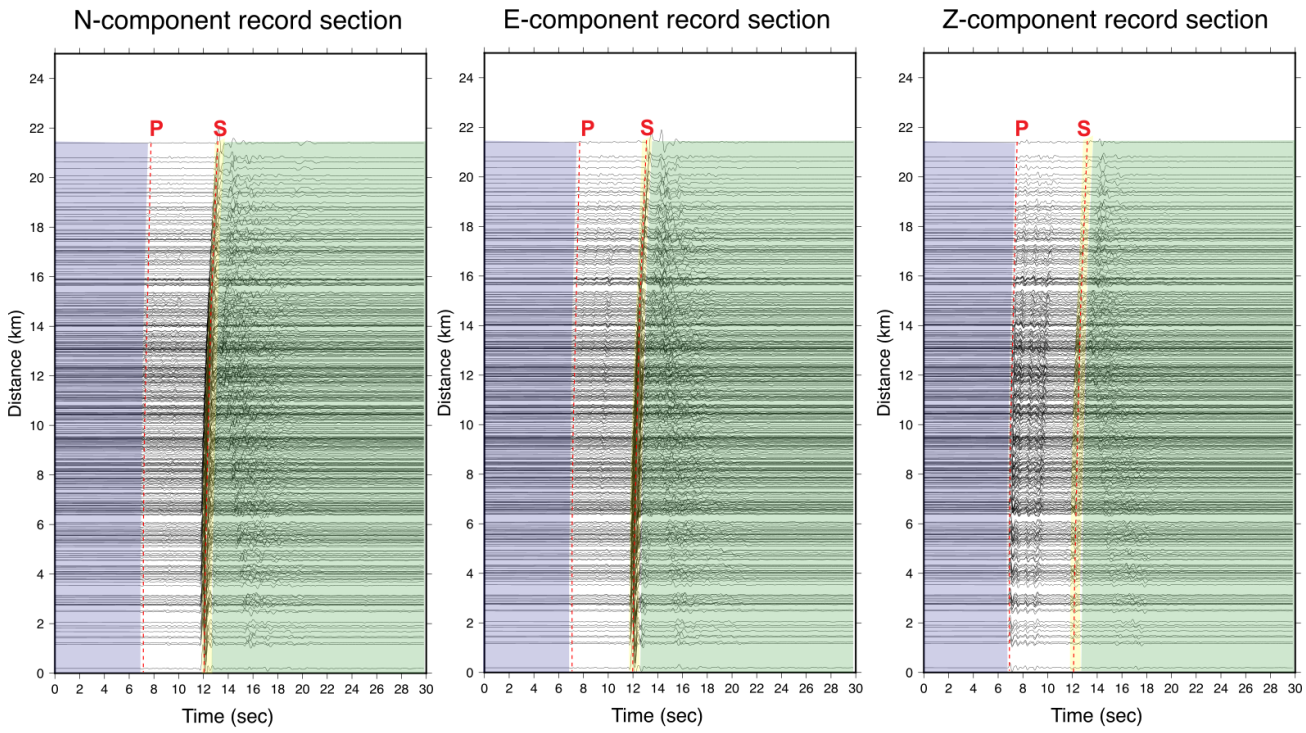

Figure 6 Seismograms for a M4.1 shear source. Arrival times of P and S direct waves are shown at the locations of dashed red curves. Converted phases arrive between these two direct waves. The areas highlighted in blue and green are windowed out prior to an adjoint run for an S to P imaging function, and the areas highlighted in yellow and green are windowed out prior to an adjoint run for a P to S imaging function.

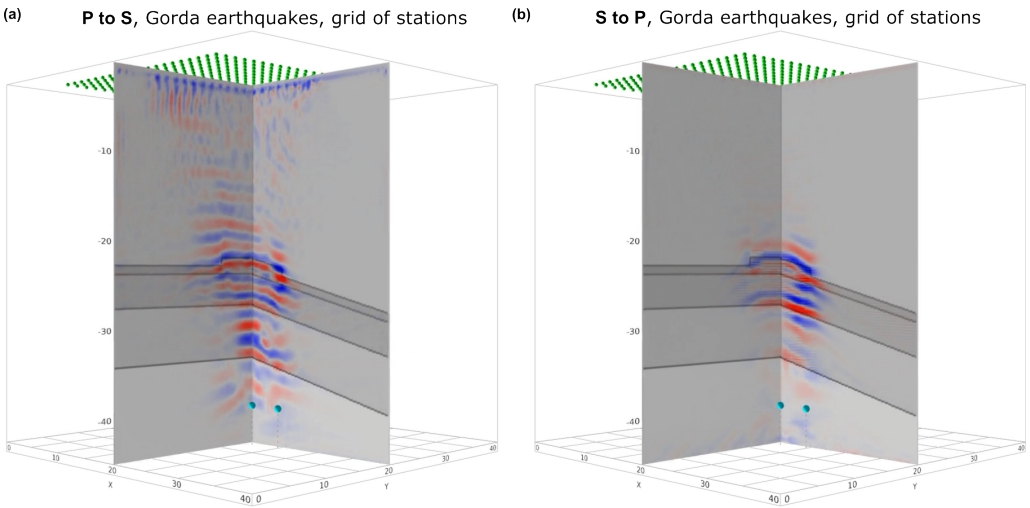

Figure 7 Stacked imaging functions for Gorda earthquake seismic sources obtained with a grid of 400 seismic stations. $P \rightarrow S$ imaging function (a) and $S \rightarrow P$ imaging function (b).

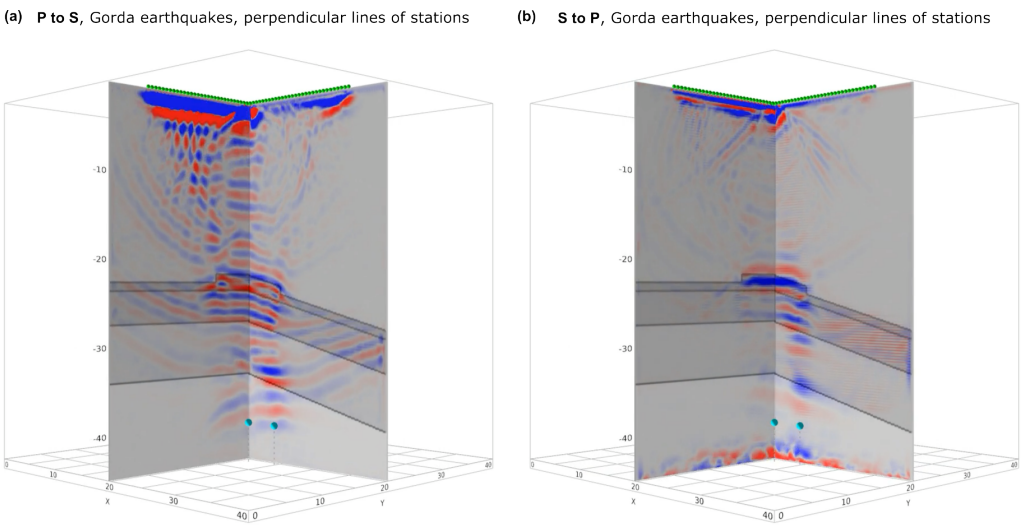

Figure 8 Stacked imaging functions for Gorda earthquake seismic sources obtained with two perpendicular lines of seismic stations. $P \rightarrow S$ imaging function (a) and $S \rightarrow P$ imaging function (b).

each other. The $P \rightarrow S$ imaging function appears similar to the imaging function obtained using data from two perpendicular lines of seismic stations and isotropic earthquake sources, shown in Figure 4(b): the imaging function is well recovered near the center of the domain, in the resolvable region, but significant artifacts are present outside that region. The $S \rightarrow P$ imaging function is more clean, with fewer artifacts outside the resolvable region, but again a smaller region is resolved, consistent with the narrower region illuminated by higher take-off angles of direct S waves. Together, these examples demonstrate that our converted-wave reverse time migration is capable of recovering informative, high-resolution imaging functions in subduction zone regions given realistic earthquake sources and feasible station geometries.

4 Discussion

The examples that we have presented demonstrate our converted-wave reverse time migration technique can fill the need for fine-scale structural models of subduction zone regions via the calculation of informative high-resolution 3D imaging functions in a model domain that features reasonable station geometry and realistic earthquakes. The imaging functions shown in this study are capable of recovering high-resolution information about multiple impedance contrasts at depths of up to 40 km, over an area of approximately 400 sq km, using data from just a few realistic earthquakes and relatively sparse seismic arrays. Consequently, our technique is immediately applicable to subduction zone regions where dense seismic datasets already exist, and we anticipate that it will be applicable to seismic datasets that are expected to be collected in the near future, such as the SZ4D MegaArray (Hilley et al., 2022).

One important component of real-world applicability is the computational efficiency of our implementation. As we have discussed, we've already optimized I/O and developed parallelized workflows to greatly improve the efficiency of our method. During the development process, we have chosen to output the full wavefield data so we can visualize the P and S wavefields, and gain a thorough understanding of how our imaging technique is inferring discontinuity locations from the data. Thanks to our optimized I/O routine, this decision has not incurred prohibitive computational costs. However, computational costs may be reduced further in the future through the implementation of a workflow that calculates imaging functions for individual earthquakes without the need to output large wavefield data as an intermediate step.

The high frequency content of S waves leads to computational challenges which are not so easily overcome. As we have mentioned, high frequency seismic data tend to lead to artifacts at the edges of mesh elements unless the mesh spacing is very fine. This is particularly important when S to P images are desired, due to the higher frequency content of S waves. Consideration of this issue is likely to be important in real world situations where the S to P observed converted phases are strong and an S to P image may be targeted in an imaging project. In that case, as we have shown, the problem remains tractable, but greater computational resources may be required, and caution should be exercised in interpretation of images which may include high-resolution artifacts. It should also be anticipated that a smaller region will be resolved by the $S \rightarrow P$ imaging function. However, because $S \rightarrow P$ imaging functions are able to recover fine-scale structure at exceptionally high resolution, it is worthwhile to overcome these challenges when large amplitude S to P converted waves are present in observed data.

Acknowledgements

Leah Langer was supported by a USGS Mendenhall postdoctoral fellowship. Computations for imaging functions were performed on the NASA Pleiades supercomputer. Any use of trade, firm or product names is for descriptive purposes only and does not imply endorse-

ment by the U.S. Government. We thank Ian Stone, David Schlaphorst and an anonymous reviewer whose feedback greatly improved this manuscript.

Data and code availability

No new data were generated or analyzed in support of this research. The SPECFEM3D seismic wave propagation code is available from https://github.com/SPECFEM/specfem3d. Meshes were produced with the Cubit meshing toolkit, https://cubit.sandia.gov/, and converted to SPECFEM3D format with MeshAssist, https://github.com/homnath/MeshAssist/tree/master. The synthetic data produced for this study are available as a USGS data release (Langer, 2024).

Competing interests

The authors state that they have no competing interests.

References

Bangs, N. L., Morgan, J. K., Bell, R. E., Han, S., Arai, R., Kodaira, S., Gase, A. C., Wu, X., Davy, R., Frahm, L., Tilley, H. L., Barker, D. H. N., Edwards, J. H., Tobin, H. J., Reston, T. J., Henrys, S. A., Moore, G. F., Bassett, D., Kellett, R., Stucker, V., and Fry, B. Slow slip along the Hikurangi margin linked to fluid-rich sediments trailing subducting seamounts. *Nature Geoscience*, 16(6): 505–512, 2023. doi: 10.1038/s41561-023-01186-3.

Bassett, D., Shillington, D. J., Wallace, L. M., and Elliott, J. L. Variation in slip behaviour along megathrusts controlled by multiple physical properties. *Nature Geoscience*, 18(1):20–31, 2025. doi: 10.1038/s41561-024-01617-9.

Bostock, M., Rondenay, S., and Shragge, J. Multiparameter two-dimensional inversion of scattered teleseismic body waves, 1, Theory for oblique incidence. *J. Geophys. Res.*, 106: 30785–30796, 2001.

Carbotte, S. M., Boston, B., Han, S., Shuck, B., Beeson, J., Canales, J. P., Tobin, H., Miller, N., Nedimovic, M., Tréhu, A., Lee, M., Lucas, M., Jian, H., Jiang, D., Moser, L., Anderson, C., Judd, D., Fernandez, J., Campbell, C., Goswami, A., and Gahlawat, R. Subducting plate structure and megathrust morphology from deep seismic imaging linked to earthquake rupture segmentation at Cascadia. *Science Advances*, 10(23):eadl3198, 2024. doi: 10.1126/sciadv.adl3198.

Christensen, N. I. Poisson's ratio and crustal seismology. *Journal of Geophysical Research: Solid Earth*, 101(B2):3139–3156, 1996. doi: 10.1029/95JB03446.

Contreras-Reyes, E. and Carrizo, D. Control of high oceanic features and subduction channel on earthquake ruptures along the Chile–Peru subduction zone. *Physics of the Earth and Planetary Interiors*, 186(1):49–58, 2011. doi: 10.1016/j.pepi.2011.03.002.

den Hartog, S. A. M. and Spiers, C. J. A microphysical model for fault gouge friction applied to subduction megathrusts. *Journal of Geophysical Research: Solid Earth*, 119(2):1510–1529, 2014. doi: 10.1002/2013JB010580.

Du, Y., Li, Y., Yang, J., Cheng, A., and Fang, X. Source-free converted-wave reverse time migration: Formulation and limitations. *Geophysics*, 84:S17–S27, 2019.

Duan, B. Effects of low-velocity fault zones on dynamic ruptures with nonelastic off-fault response. *Geophysical Research Letters*, 35(4), 2008. doi: 10.1029/2008GL033171.

Duan, Y. and Sava, P. C. Scalar imaging condition for elastic reverse-time migration. *Geophysics*, 80:S127–S136, 2015.

Eberhart-Phillips, D. and Reyners, M. Plate interface properties in the northeast Hikurangi subduction zone, New Zealand, from converted seismic waves. *Geophysical Research Letters*, 26(16): 2565–2568, 1999. doi: 10.1029/1999GL900567.

Ghosh, A., Vidale, J. E., Sweet, J. R., Creager, K. C., and Wech, A. G. Tremor patches in Cascadia revealed by seismic array analysis. *Geophysical Research Letters*, 36(17), 2009. doi: 10.1029/2009GL039080.

Gomberg, J., Ludwig, K., Bekins, B., Brocher, T., Brock, J., Brothers, D., Chaytor, J., Frankel, A., Geist, E., Haney, M., Hickman, S., Leith, W., Roeloffs, E., Schulz, W., Sisson, T., Wallace, K., Watt, J., and Wein, A. Reducing risk where tectonic plates collide—U.S. Geological Survey subduction zone science plan: U.S. Geological Survey circular 1428, 2017. doi: 10.3133/cir1428.

Gong, J. and McGuire, J. J. Constraints on the geometry of the subducted Gorda plate From converted phases generated by local earthquakes. *Journal of Geophysical Research: Solid Earth*, 126 (2):e2020JB019962, 2021. doi: 10.1029/2020JB019962.

Guo, H., McGuire, J. J., and Zhang, H. Correlation of porosity variations and rheological transitions on the southern Cascadia megathrust. *Nature Geoscience*, 14(5):341–348, 2021. doi: 10.1038/s41561-021-00740-1.

Herath, P. and Audet, P. Fluid upwelling across the Hikurangi subduction thrust during deep slow-slip earthquakes. *Communications Earth & Environment*, 5(1):697, 2024. doi: 10.1038/s43247-024-01864-z.

Hilley, G. E., Brodsky, E. E., Roman, D., Shillington, D. J., Brudzinski, M., Behn, M. Tobin, H., and the SZ4D RCN. SZ4D implementation plan. *Stanford Digital Depository*, 2022. doi: 10.25740/hy589fc7561.

Horleston, A. and Helffrich, G. Constraining sediment subduction: A converted phase study of the Aleutians and Marianas. *Earth and Planetary Science Letters*, 359-360:141–151, 2012. doi: 10.1016/j.epsl.2012.10.019.

Huang, Y. and Ampuero, J.-P. Pulse-like ruptures induced by low-velocity fault zones. *Journal of Geophysical Research: Solid Earth*, 116(B12), 2011. doi: 10.1029/2011JB008684.

Hutchison, A. A. and Ghosh, A. Ambient Tectonic Tremor in the San Jacinto fault, near the Anza gap, Detected by multiple mini seismic arrays. *Bulletin of the Seismological Society of America*, 107(5):1985–1993, 09 2017. doi: 10.1785/0120160385.

Kato, A., Iidaka, T., Ikuta, R., Yoshida, Y., Katsumata, K., Iwasaki, T., Sakai, S., Thurber, C., Tsumura, N., Yamaoka, K., Watanabe, T., Kunitomo, T., Yamazaki, F., Okubo, M., Suzuki, S., and Hirata, N. Variations of fluid pressure within the subducting oceanic crust and slow earthquakes. *Geophysical Research Letters*, 37 (14), 2010. doi: 10.1029/2010GL043723.

Komatitsch, D. and Tromp, J. Spectral-element simulations of global seismic wave propagation—I. Validation. *Geophysical Journal International*, 149(2):390–412, 05 2002a. doi: 10.1046/j.1365-246X.2002.01653.x.

Komatitsch, D. and Tromp, J. Spectral-element simulations of global seismic wave propagation—II. Three-dimensional models, oceans, rotation and self-gravitation. *Geophysical Journal International*, 150(1):303–318, 2002b. doi: 10.1046/j.1365-246X.2002.01716.x.

Kutschera, F., Gabriel, A.-A., Wirp, S. A., Li, B., Ulrich, T., Abril, C., and Halldórsson, B. Linked and fully coupled 3D earthquake dynamic rupture and tsunami modeling for the Húsavík–Flatey Fault Zone in North Iceland. *Solid Earth*, 15(2):251–280, 2024. doi: 10.5194/se-15-251-2024.

Langer, L. Synthetic seismogram data for 3D converted wave reverse time migration imaging of subduction zone structure: U.S. Geological Survey data release, 2024. doi: 10.5066/P13M75JZ.

Langer, L., Pollitz, F. F., and McGuire, J. J. Converted-wave reverse time migration imaging in subduction zone settings. *Geophysical Journal International*, 235(2):1384–1402, 08 2023. doi: 10.1093/gji/ggad308.

Li, H. and Li, J. Elastic Transmitted Wave Reverse Time Migration for Imaging Earth's Interior Discontinuities: A Numerical Study. *Bulletin of the Seismological Society of America*, 112(5): 2231–2256, 06 2022. doi: 10.1785/0120210325.

Li, J., Shillington, D. J., Bécel, A., Nedimović, M. R., Webb, S. C., Saffer, D. M., Keranen, K. M., and Kuehn, H. Downdip variations in seismic reflection character: Implications for fault structure and seismogenic behavior in the Alaska subduction zone. *Journal of Geophysical Research: Solid Earth*, 120(11):7883–7904, 2015. doi: 10.1002/2015JB012338.

Liu, Y. Numerical simulations on megathrust rupture stabilized under strong dilatancy strengthening in slow slip region. *Geophysical Research Letters*, 40(7):1311–1316, 2013. doi: 10.1002/grl.50298.

Lotto, G. C., Jeppson, T. N., and Dunham, E. M. fully coupled simulations of megathrust earthquakes and tsunamis in the Japan trench, Nankai trough, and Cascadia subduction zone. *Pure and Applied Geophysics*, 176:4009 – 4041, 2019. doi: 10.1007/s00024-018-1990-y.

Madden, E. H., Bader, M., Behrens, J., van Dinther, Y., Gabriel, A.-A., Rannabauer, L., Ulrich, T., Uphoff, C., Vater, S., and van Zelst, I. Linked 3-D modelling of megathrust earthquake-tsunami events: from subduction to tsunami run up. *Geophysical Journal International*, 224(1):487–516, 10 2020. doi: 10.1093/gji/ggaa484.

Nedimovic, M. R., Hyndman, R. D., Ramachandran, K., and Spence, G. D. Reflection signature of seismic and aseismic slip on the northern Cascadia subduction interface. *Nature*, 424(6947): 416–420, 2003. doi: 10.1038/nature01840.

Nikulin, A., Levin, V., and Park, J. Receiver function study of the Cascadia megathrust: Evidence for localized serpentinization. *Geochemistry, Geophysics, Geosystems*, 10(7), 2009. doi: 10.1029/2009GC002376.

Preston, L. A., Creager, K. C., Crosson, R. S., Brocher, T. M., and Trehu, A. M. Intraslab earthquakes: Dehydration of the Cascadia slab. *Science*, 302(5648):1197–1200, 2003. doi: 10.1126/science.1090751.

Ryberg, T., Haberland, C., Fuis, G. S., Ellsworth, W. L., and Shelly, D. R. Locating non-volcanic tremor along the San Andreas Fault using a multiple array source imaging technique. *Geophysical Journal International*, 183(3):1485–1500, 12 2010. doi: 10.1111/j.1365-246X.2010.04805.x.

Shabelansky, A., Malcolm, A., and Fehler, M. Converted-wave seismic imaging: Amplitude-balancing source-independent imaging conditions. *Geophysics*, 82:S99–S109, 2017.

Shang, X., de Hoop, M. V., and van der Hilst, R. D. Beyond receiver functions: Passive source reverse time migration and inverse scattering of converted waves. *Geophys. Res. Lett.*, 39:L15308, doi:10.1029/2012GL052289, 2012.

Shiraishi, K., Moore, G. F., Yamada, Y., Kinoshita, M., Sanada, Y., and Kimura, G. Seismogenic zone structures revealed by improved 3-D seismic images in the Nankai trough off Kumano. *Geochemistry, Geophysics, Geosystems*, 20(5):2252–2271, 2019. doi: 10.1029/2018GC008173.

Takemura, S., Furumura, T., and Maeda, T. Scattering of high-frequency seismic waves caused by irregular surface topography and small-scale velocity inhomogeneity. *Geophysical Journal International*, 201(1):459–474, 02 2015. doi: 10.1093/gji/ggv038.

Thakur, P., Huang, Y., and Kaneko, Y. Effects of low-velocity fault damage zones on long-term earthquake behaviors on mature strike-slip faults. *Journal of Geophysical Research: Solid Earth*, 125(8):e2020JB019587, 2020. doi: 10.1029/2020JB019587.

Ward, K. M., Lin, F., and Schmandt, B. High-resolution receiver function imaging across the Cascadia subduction zone Using a dense nodal array. *Geophysical Research Letters*, 45(22): 12,218–12,225, 2018. doi: 10.1029/2018GL079903.

Zou, P., Cheng, J., Wang, T., and Zhang, H. Three-dimensional teleseismic elastic reverse-time migration with deconvolution imaging condition and its application to southwest Japan. *Geophysical Research Letters*, 51(8):e2023GL107446, 2024. doi: 10.1029/2023GL107446.